Title

Shallow Crustal Shear Velocity and Vp/Vs Across Southern California: Joint Inversion of Short-Period Rayleigh Wave Ellipticity, Phase Velocity, and Teleseismic Receiver Functions

Journal

Geophysical Research Letters, 48(15)

ISSN

0094-8276

Authors

Berg, Elizabeth M
Lin, Fan-Chi
Schulte-Pelkum, Vera
et al.

Publication Date

2021-08-01

DOI

10.1029/2021gl092626

Peer reviewed

Shallow Crustal Shear Velocity and Vp/Vs across Southern California: Joint Inversion of Short-Period Rayleigh Wave Ellipticity, Phase Velocity, and Teleseismic Receiver Functions

[1]Elizabeth M. Berg, [1]Fan-Chi Lin, [2]Vera Schulte-Pelkum, [1]Amir Allam, [3]Hongrui Qiu, and [1]Konstantinos Gkogkas

[1]Department of Geology and Geophysics, University of Utah, Salt Lake City, Utah, USA

[2]Cooperative Institute for Research in Environmental Sciences and Department of Geological Sciences, University of Colorado Boulder, Boulder, Colorado, USA

[3]Department of Earth, Environmental and Planetary Sciences, Rice University, Houston, Texas, USA

Key Points:

- We present near-surface Vp/Vs and upper crust shear velocity models of Southern California via Markov Chain Monte Carlo joint inversion.
- Joint inversion uses receiver functions, and ambient-noise derived, short-period, Rayleigh-wave phase velocity and ellipticity (H/V) data.
- Vp/Vs ratios fit fluid-saturated sediments in major basins and are otherwise low, implying fracturing and/or groundwater undersaturation.

Abstract

Near-surface seismic velocity structure plays a critical role in ground motion amplification during large earthquakes. In particular, the local Vp/Vs ratio strongly influences the amplitude of Rayleigh waves. Previous studies have separately imaged 3D seismic velocity and Vp/Vs ratio at seismogenic depth, but lack regional coverage and/or fail to constrain the shallowest structure. Here, we combine three datasets with complementary sensitivity in a Bayesian joint inversion for shallow crustal shear velocity and near-surface Vp/Vs ratio across Southern California. Receiver functions – including with an apparent delayed initial peak in sedimentary basins, and long considered a nuisance in receiver function imaging studies – highly correlate with short-period Rayleigh wave ellipticity measurements and require the inclusion of a Vp/Vs parameter. The updated model includes near-surface low shear velocity more in line with geotechnical layer estimates, and generally lower than expected Vp/Vs outside the basins suggesting widespread shallow fracturing and/or groundwater undersaturation.

1 Introduction

Southern California has a long history of seismic imaging studies at all scales, from regional tomography (e.g., Fang et al., 2016; Lee et al., 2014; Qiu et al., 2019; Tape et al., 2009), to local-scale basin and fault-zone structure (e.g., Allam et al., 2014; Fuis et al., 2001, 2017; Süss & Shaw, 2003), and multi-scale joint inversions of multiple datasets (Berg et al., 2018; Bennington et al., 2015). A primary motivation for these works is the significant seismic hazard posed by the San Andreas fault system, and the related need for physics-based hazard assessment of the region (Graves et al., 2011; Vidale & Helmberger, 1988). For the past 25 years, the Southern California Earthquake Center has developed and maintained multiple Community Velocity Models (CVM) with seismic hazard assessment as one of the explicit goals (Chen et al., 2007; Lee et al., 2014; Magistrale et al., 1996; Plesch et al., 2007; Suss & Shaw, 2003; Tape et al., 2009). Despite the long history and contributions from a large community of researchers, there are still several shortcomings to the Southern California CVM. In particular, near-surface velocity structure (<1km depth), and corresponding ratio of compressional to shear velocity (Vp/Vs), remain poorly resolved at regional scales. Shallow structure is well-known to exert strong influence on the co-seismic ground motion (e.g., Graves et al., 2011), while local Vp/Vs ratio can produce amplification by a factor of three (Yang & Sato, 2000) even for sites already subject to amplification due to low local shear wave velocity (e.g., basins). To address these issues, several versions of the CVM (Lee et al., 2014; Plesch et al., 2007) include a shallow layer constrained by very local-scale geotechnical studies; this ad hoc layer creates various edge effects and other artifacts (Figure S1) in the model and wavefield simulations (Taborda et al., 2016).

Measurements of Vp/Vs for southern California generally fall into three categories: low-resolution volumetric averages (e.g., Allam et al., 2014; Hauksson, 2000; Lin et al., 2007), localized measurements at seismogenic depth (e.g., Lin & Shearer, 2007; Lin, 2020; Zhang & Lin, 2014), and localized near-surface measurements from boreholes (Boore et al., 2003; Shaw et al., 2015 and references therein) or temporary seismic arrays (e.g., Murphy et al., 2010). The latter category is the most important for seismic hazard, but the extremely local nature is difficult to implement in physics-based assessments. Though there are many models which independently constrain Vp and/or Vs (e.g., Lee et al., 2014; Lin et al., 2010; Schmandt & Humphreys, 2010; Tanimoto & Sheldrake, 2002), naïvely dividing Vp by Vs models obtained with different data of differing resolution results in extreme inaccuracies and numerical artifacts (e.g., Allam & Ben-Zion, 2012). In addition, because most methods measure Vp/Vs at depth from earthquake sources, they lead to overestimations of Vp/Vs ratio under near-surface stress conditions (Zaitsev et al., 2017).

In order to provide a model with resolution of Vs and Vp/Vs in the upper few km, we combine the complementary sensitivities of Rayleigh-wave phase velocities (upper crust), ellipticity (upper few km), and the initial pulse of teleseismic receiver functions (shallow Vp/Vs ratio and shallow interfaces) to create a self-consistent model at the regional scale across southern California. The idea to combine receiver functions and surface wave data in a Bayesian joint inversion to determine Vs and Vp/Vs is relatively new (Dreiling et al., 2020; Ojo et al., 2019), and only recently shown to be promising in resolving near-surface Vs and Vp/Vs in sediments (Li et al., 2019). By including Vp/Vs as a parameter we are able to fit receiver functions on a regional scale for the first time across 231 Southern California stations, including in basins where receiver functions have long been discarded as nuisance signals or "corrected" with ad-hoc models, as reverberations overprint Moho and other crustal signatures (e.g., Yeck et al., 2013). The results, presented in Section 3 and discussed in Section 4 below, include a map of Vp/Vs across the region and 3D shear-velocity (Vs) model with very low near-surface velocities in basins more in line with previous measurements of shallow, local Vs.

2 Data and Methods

2.1 Ambient Noise Surface Wave Measurements

We process three-component broadband stations (Figure 1a) identically to Berg et al. (2018), except to apply an initial band-pass filter to all continuous recordings of 0.5 to 170 s periods (instead of 5 to 150 s) to avoid frequency-band edge effects. We retain relative amplitude information during cross-correlation to measure Rayleigh-wave ellipticity, or horizontal-to-vertical (H/V) ratios (Berg et al., 2018; Lin et al., 2014). The isotropic H/V ratio and uncertainty are determined from the mean and standard deviation of the mean, respectively, for each station with at least 20 measurements remaining after removing outliers; more details can be found in Berg et al. (2018). In addition to Rayleigh-wave H/V ratio measurements from 6 to 10 s periods, we use 3 to 10 s periods Rayleigh-wave phase velocities from previous ambient-noise-based eikonal tomography (Qiu et al., 2019) extracted at the inversion grid point nearest to each station.

2.2 Receiver Functions

We obtain receiver functions, which capture near-station structural contrasts via P to S conversions and reverberations (Langston, 1977; Ligorria & Ammon, 1999; Vinnik, 1977). We analyze P and P_{diff} arrivals and their coda from all teleseismic events from January 2004 to August 2020 with Mw > 5.1 and epicentral distances 28º to 150º via the time domain iterative method of Ligorria and Ammon (1999) with a Gaussian filter factor of 3 (i.e., a pulse width of 1 s). We apply automated processing based on previous work (Schulte-Pelkum & Mahan, 2014a; 2014b) including basic quality control steps, correction to a standard ray parameter of 0.06 s/km, and receiver function binning by back-azimuth; see Schulte-Pelkum & Mahan (2014a; 2014b) for details. The final isotropic receiver function consists of the mean of all back-azimuths for stations with a minimum of 14 individual receiver functions. To focus on shallow structure, we only consider the first 2 s of each receiver function. In sedimentary basins the initial pulse is delayed due to the superposition of direct P and larger amplitude sediment Ps conversions, as the large velocity contrast at the sediment base refracts rays to nearly-vertical incidence (Li et al., 2019; Schulte-Pelkum et al., 2017). Larger delay times of the initial receiver function pulse are clearly observed in basin stations (Figure 1b).

2.3 Monte Carlo Joint Inversion

We leverage the complementary sensitivities of the Rayleigh phase velocity, H/V ratio, and receiver function datasets through a Markov Chain Monte Carlo (MCMC) joint inversion at each station to efficiently and effectively explore the parameter space, quantify model uncertainty, and avoid local minima (Berg et al., 2018; Roy & Romanowicz, 2017; Shen & Ritzwoller, 2016). Our MCMC model for each station consists of a top linear layer over a crustal layer with initial Vs from Berg et al. (2018) and initial Vp/Vs from the Brocher (2005) empirical relationship. Crustal Vs is parameterized with ten cubic B-splines with asymmetric density higher in the shallower crust (Berg et al., 2018). We perturb eight free parameters (Table S1), including the Vs in the top linear layer and the upper four B-splines in the crust, as well as the thickness and Vp/Vs in the top linear layer. The a priori distribution is formed by Gaussian probability with empirically chosen widths to fully sample the model space (see Table S1). We impose three prior constraints: a maximum Vs of 4.9km/s, a positive jump from the bottom of the top linear layer into the crustal layer, and a Vp/Vs ratio greater than 1.

The inversion explores the a priori distribution following the Metropolis algorithm (Shen et al., 2012) with misfit characterized as root-mean-square between data and model predictions with empirically chosen weights of 30%, 30%, and 40% for phase velocities, H/V ratios, and receiver functions respectively. Models with misfit less than 1.5 of the minimum misfit are included in the posterior distribution, and we require the posterior to contain more than 300 models for the station to be included in the final results. On average, there are ~2000 models in each posterior. Details about the number of iterations, avoiding the edges of prior distributions, and data uncertainties can be found in previous works (Berg et al., 2018, 2020; Shen et al., 2012).

Our final model is formed by the mean of the model parameters in the posterior, except in cases where the mean results in a misfit value higher than that in the posterior (i.e., higher than 1.5 times the absolute minimum misfit). This generally occurs where the posterior models have bimodal distribution, and in these instances our final model is the model with minimum misfit.

Figure 2 shows the 1-D inversion result for station RUS (star, Figure 1c), including the full prior and posterior distributions and data fits, and the effects of the inclusion of the receiver function data. When the receiver function data (Figure 2c) are not used, the shallow structure and Vp/Vs ratio (Figure 2a, 2b) are poorly constrained by the inversion, though the Rayleigh wave ellipticity and phase velocity (Figure 2d, 2e) are equally well-fit in either case. By incorporating receiver functions, not only do we gain better constraint on the near-surface layered interface structure (Allam et al., 2017; Langston, 1979; Shen & Ritzwoller, 2016; Ward & Lin, 2018), but the complementary dataset results in a tighter distribution of results in both the Vs and the Vp/Vs model space (Figure 2a, 2b). Thus receiver function data are most sensitive to the near-surface velocity and Vp/Vs ratio, justifies the inclusion of the latter, and demonstrates receiver function utility when included in this inversion.

3 Results

3.1 Rayleigh-Wave Ellipticity and Receiver Function Measurements

As in previous work (Berg et al., 2018), as 7 s period (Figure 1a) we observe high H/V ratios in sedimentary basins including the Los Angeles, Central Valley, Salton Trough, and Ventura basins; we observe low H/V ratios in mountainous regions such as the Sierra Nevada and Peninsular Ranges. The surface patterns of soft sediment compared to hard bedrock are also evident from the Wills & Clahan (2006) Vs30 map of the region (Figure 1c).

From the map of receiver function initial pulse delay time (Figure 1b), we see similar patterns to those of the H/V ratio map (Figure 1a) and the Vs30 map (Figure 1c). We observe earlier arrivals of the initial receiver function pulse in crystalline rock, including in the Peninsular and Sierra Nevada Ranges, and later arrivals in sedimentary basins, including the Los Angeles basin and the Salton Trough. The superposition of direct P and larger amplitude P-to-S conversions in sedimentary basins, from the bedrock interface and reverberations within, yields delayed and more-intricate initial pulses in the receiver functions (Li et al., 2019; Schulte-Pelkum et al., 2017; Yeck et al., 2013). Although typically ignored for their complexity (e.g., Allam et al., 2017), we directly compare the receiver function delay times to the short-period H/V ratios as both have shallow sensitivity. We observe strong correlation values (mean correlation coefficient 0.76) between 6-10 s period H/V ratios and receiver function delay times; higher H/V ratios correspond to later receiver function initial pulse times (Figure 1d), which in turn correspond to lower Vs30 areas.

3.2 Shear Velocity Model

Figures 3a and 3b show the Vs velocity MCMC inversion result at 0 km and 1 km depths, respectively, interpolated onto the underlying map, with a cross-section shown in Figure 3d. Major features include low-Vs sedimentary basins such as the Los Angeles basin, Central Valley, Ventura basin, and Salton Trough. We also observe the high-Vs Peninsular and Sierra Nevada Ranges. Less prominent features include the Indian Wells Valley (Figures 3a and 3b) east of the Sierra Nevada, shallow Antelope Valley (Figure 3a) in the northwest corner of the Mojave desert, and the low-Vs Coast Ranges (Figure 3a). The northwest section of the Eastern California Shear Zone (ECSZ; Figure 3a) is observed as a broad low velocity zone at the surface, and strong across-fault contrasts in velocity are observed on the southern San Andreas, San Jacinto, and Elsinore faults (Figures 3a and 3b). In comparison to our previous Berg et al. (2018) model (i.e., our starting model), we have stronger constraint to the near-surface (see Figure S2 for the standard deviation of the posterior, and Figure S3 for misfits) with Vs values slower in areas of soft sediments (e.g., Salton Trough, LA and Central Valley basins) and faster in regions of crystalline rock (e.g., Sierra Nevada and Peninsular Ranges). A direct comparison of starting (red triangles, Figure 2a) to final model (yellow squares, Figure 2a), shows that the most prominent changes occur in the upper few km.

Further direct comparison to the CVMS are provided in Figure S1, where the impact of each of these geologic regions and similarities of our model results are visible.

In Figure 3c we show depth to Vs of 3km/s as an approximate basin depth map, based on the empirical Vp/Vs relationship (Brocher, 2005) and previous observations in the LA basin (Süss & Shaw, 2003). We observe a greater depth to 3km/s in the southeast portion of the LA and Ventura basins, and mid-range depths for the Central Valley and in the Salton Trough. This (Figure 3c, Figure S1a) agrees with previous studies (Berg et al., 2018; Fletcher & Erdem, 2017; Fliedner et al., 2000; Fuis et al., 2017; Han et al., 2016; Livers et al., 2012; Ma & Clayton; 2016; Magistrale et al., 1996). The Antelope Valley and Indian Wells Valley are shallower, fitting previous active-source studies (Lutter et al., 2004; Tape et al., 2010).

3.3 Vp/Vs in the Near Surface

While Vp/Vs in the top linear layer is resolved for every station, we analyze only those stations with a prominent layer thickness (>0.75 km) and with low normalized standard deviation of the Vp/Vs in the posterior (<0.15) to avoid including less reliable results. Figure 4a shows the Vp/Vs at stations satisfying these criteria, and the interpolated map. Figure 4b shows a scatter plot of the top linear layer average Vs compared to Vp/Vs value (circles) and the Brocher (2005) estimate (line). We observe high scatter around the Brocher-predicted Vp/Vs value skewed towards lower Vp/Vs (Figure 4b), particularly for areas with higher Vs values. Figure S4 shows the map of the normalized standard deviation of Vp/Vs and map-view of average Vs in the top linear layer.

We observe higher Vp/Vs in the Salton Trough, eastern LA basin, Central Valley, Indian Wells Valley, Antelope Valley, and in the ESCZ with corresponding slower sediments. We observe lower Vp/Vs in the Sierra Nevada mountains, in the center of the Mojave desert, and in the Peninsular Ranges. Additionally, we see a transition from higher

Vp/Vs near the San Andreas fault to low Vp/Vs along the San Jacinto and Elsinore faults. These observations are consistent with previous studies (Fang et al., 2019; Lin et al., 2007), and discussed in detail in the following section.

4 Discussion

4.1 Mountains and Mojave Desert

Compared to Berg et al. (2018), we observe faster near-surface Vs values in the Sierra Nevada and Peninsular Ranges (Figures 3a, 3b, and S4), similar to the CVMS geotechnical layer (GTL) (Shaw et al., 2015). Though the Vp/Vs ratio of rocks can vary significantly with fluid content and fracture density (Shearer, 1988; Karato & Jung, 1998), Christensen (1996) suggests that composition controls the general properties of igneous rock; felsic (e.g., granite) rocks have relatively low Vp/Vs ratio (<1.7) and high silica content (>65%), while mafic (e.g., basalt) rocks have higher Vp/Vs ratios (>1.8) and lower silica content (<45%). In the Sierra Nevada Range, we observe lower Vp/Vs consistent with Cretaceous granitic rocks (Irwin, 1990) at the surface and previous studies (Hauksson, 2000; Lin et al., 2007; Murphy et al., 2010). Consistent to previous studies (Fang et al., 2019; Hauksson, 2000), we resolve, in the southernmost portion of our study, the northern extent of the complex mafic Peninsular Ranges batholith containing an abundance of gabbros (Gastil et al., 1975; Hauksson, 2000; Kimbrough & Grove, 2005; Langenheim & Jachens, 2000; Wetmore et al., 2003) with corresponding relatively higher (~1.8) Vp/Vs ratios. We also observe the transition to the northeast into more quartz-rich granitic material (Gastil et al., 1975; Hauksson, 2000; Kimbrough & Grove, 2005; Wetmore et al., 2003), including into the fast-Vs low-Vp/Vs Cretaceous plutons (Morton & Kennedy, 2005) between the Elsinore and San Jacinto faults. Relatively low Vp/Vs ratios in the Mojave Desert between Antelope Valley (previously observed by Hauksson, 2000 & Murphy et al., 2010) and the ECSZ likely correspond to

Precambrian metamorphic and plutonic rocks with values consistent to lab measurements (McCaffree Pellerin & Christensen, 1998).

Similar to previous studies, we observe higher Vp/Vs (Figure 4a) in portions of the San Andreas fault (Fang et al., 2019; Murphy et al., 2010) and in the ECSZ (Hauksson, 2000; Lin et al., 2007) where slower Vs is also observed (Figure 3a). S-waves are particularly sensitive to reduction in velocity within a fault damage zone due to the high fracture density (Catchings et al., 2014, 2020; Mitchell & Faulkner, 2009), as observed along the Mojave section of the San Andreas Fault (Fang et al., 2019; Murphy et al., 2010). Similarly, the ECSZ contains low-Vs and high-Vp/Vs which we interpret as widespread aligned fractures created by the broad region of strike-slip deformation (Sauber et al., 1986).

More generally in our model, stations outside of sedimentary basins have low Vp/Vs (< 1.75) ratios (Figures 4a and 4b). While these values are lower than anticipated from previous imaging (Hauksson, 2000) and laboratory (Christensen, 1996) studies, recent work (Zaitsev et al., 2017) shows that low Vp/Vs and a negative Poisson ratio (Vp/Vs < 1.42) is not an exotic result and has been observed in a significant portion of experimental data samples (~45%) at low confining stress (i.e., surface conditions). Previous southern California imaging studies have observed higher Vp/Vs ratios likely due to greater depth sensitivity (Hauksson, 2000; Lin & Shearer, 2007; Lin et al., 2007). The low Vp/Vs ratios obtained in the present model suggest widespread fracturing and/or poor consolidation with little-to-no fluid saturation (Avseth & Bachrach, 2005; Bachrach et al., 2000; Shearer, 1988) in the near-surface crust of Southern California outside of major basins.

4.2 Basins

Major basins in Southern California are clearly observed as regions of high Vp/Vs and reduced Vs (Figure 3a), lower than previous imaging work (Berg et al., 2018; Lee et al., 2014; Tape et al., 2010) and more in line with estimates of Vs30/GTL (Figure S1ffy, Shaw et al., 2015). These include the Salton Trough, Central Valley, and Los Angeles and Ventura basins. We do not observe the San Bernardino Basin – likely because of station coverage and overall shallow basement depth (Anderson et al., 2004) – but the nearby Cajon and Banning Passes are visible as low-Vs high-Vp/Vs areas.

The high Vp/Vs ratios (Figure 4a) seen in all basins are consistent with fluid-saturated measurements and observed in previous studies (Fang et al., 2019; Hauksson, 2000; Hauksson & Haase, 1997; Lin et al., 2007; Murphy et al., 2010). In the LA basin (Figure S4) we observe strong similarities in Vs to the GTL, which is well-constrained via dense borehole measurements (Shaw et al., 2015). Although we have limited horizontal resolution due to station coverage, we observe that the deepest part of the LA basin (Figure 3c) lies between the Newport-Inglewood and Whittier faults (20-50km distance in Figure 3d). This portion of the LA basin coincides with relatively higher Vp/Vs ratios, potentially related to the shallower water table (CA DWR, 2017; WRD, 2017), and is consistent to previous studies based on borehole measurements (Hauksson & Haase, 1997) and local earthquakes (Lin et al., 2007). North of the Hollywood fault, in the Santa Monica mountains between the LA and Ventura basins, we observe low Vp/Vs similar to borehole studies (Hauksson & Haase, 1997). The Santa Monica mountains contain Mesozoic igneous and metamorphic granitic rocks (Lutter et al., 2004; Murphy et al., 2010), and the region adjacent to the Hollywood fault contains granitic and dioritic plutonic rocks (Hildenbrand et al., 2001).

5 Conclusions

We apply Markov Chain Monte Carlo inversion of short-period Rayleigh-wave phase velocity and ellipticity with early-time (0-2 s) receiver functions to determine shallow Vs (<10 km) and near-surface Vp/Vs ratios. We observe Vs values near the surface that more closely resemble borehole and exploration studies in the Los Angeles basin, and higher Vs in the Peninsular and Sierra Nevada Ranges near the surface. Our low Vp/Vs ratio results outside of fluid-saturated basins correspond to mafic material in the Peninsular Ranges, felsic material in the Sierra Nevada Ranges and granitic regions, and significantly overall low Vp/Vs suggests widespread shallow fracturing and/or groundwater undersaturation.

Acknowledgements

Data are archived and distributed by the Southern California Earthquake Data Center (SCEDC; http://scedc.caltech.edu/ research-tools/waveform.html) and the IRIS Earthquake Data Center (https://ds. iris.edu/ds/nodes/dmc/). The SCEC Community Velocity Model, CVMS-4.26, is available from the Southern California Earthquake Center (https://github.com/ SCECcode/UCVMC , only available at Github). This study was supported by the Southern California Earthquake Center (awards 20058 and 17097), National Science Foundation (Grants EAR – 1753362, EAR- 1927246, EAR-1736248, and EAR-1735890), USGS award G18AP00033, Stokes-Eardley Fellowship, and a scholarship from the Onassis Foundation (Scholarship ID: F ZO 02-1/ 2018-2019). Model of 3-D shear wave velocity and surface Vp/Vs is available from IRIS Data Services Products: Earth Model Collaboration (https://doi.org/10.17611/dp/emc.2021.scabergetal.1).

References

Allam, A. A., & Ben-Zion, Y. (2012). Seismic velocity structures in the Southern California plate boundary environment from double-difference tomography. *Geophysical Journal International*, *190*(2), 1181–1196. https://doi.org/10.1111/j.1365-246X.2012.05544.x

Allam, A. A., Ben-Zion, Y., Kurzon, I., & Vernon, F. (2014). Seismic velocity structure in the hot springs and trifurcation areas of the San Jacinto fault zone, California, from double-difference tomography. *Geophysical Journal International, 198*(2), 978–999. https://doi.org/10.1093/gji/ggu176

Allam, A. A., Schulte-Pelkum, V., Ben-Zion, Y., Tape, C., Ruppert, N., & Ross, Z. E. (2017). Ten kilometer vertical Moho offset and shallow velocity contrast along the Denali fault zone from double-difference tomography, receiver functions, and fault zone head waves. *Tectonophysics, 721*, 56–69. https://doi.org/10.1016/j.tecto.2017.09.003

Anderson, M., Matti, J., & Jachens, R. (2004). Structural model of the San Bernardino basin, California, from analysis of gravity, aeromagnetic, and seismicity data. *Journal of Geophysical Research: Solid Earth*, *109*(B4). https://doi.org/10.1029/2003JB002544.

Avseth, P., & Bachrach, R. (2005). Seismic properties of unconsolidated sands: Tangential stiffness, Vp/Vs ratios and diagenesis. In *SEG Technical Program Expanded Abstracts 2005* (pp. 1473-1476). Society of Exploration Geophysicists. https://doi.org/10.1190/1.2147968

Bachrach, R., Dvorkin, J., & Nur, A. M. (2000). Seismic velocities and Poisson's ratio of shallow unconsolidated sandsSeismic Properties of Shallow Sands. *Geophysics*, *65*(2), 559-564. https://doi.org/10.1190/1.1444751

Bennington, N. L., Zhang, H., Thurber, C. H., & Bedrosian, P. A. (2015). Joint inversion of seismic and magnetotelluric data in the Parkfield Region of California using the normalized cross-gradient constraint. *Pure and Applied Geophysics*, *172*(5), 1033-1052. https://doi.org/10.1007/s00024-014-1002-9

Bensen, G. D., Ritzwoller, M. H., Barmin, M. P., Levshin, A. L., Lin, F., Moschetti, M. P., et al. (2007). Processing seismic ambient noise data to obtain reliable broad-band surface wave dispersion measurements. *Geophysical Journal International, 169*(3), 1239–1260. https://doi.org/ 10.1111/j.1365-246X.2007.03374.x

Berg, E. M., Lin, F. C., Allam, A., Qiu, H., Shen, W., & Ben-Zion, Y. (2018). Tomography of Southern California via Bayesian joint inversion of Rayleigh wave ellipticity and phase velocity from ambient noise cross-correlations. *Journal of Geophysical Research: Solid Earth*, *123*(11), 9933–9949. https://doi.org/10.1029/2018JB016269

Berg, E. M., Lin, F.-C., Allam, A., Schulte-Pelkum, V., Ward, K. M., & Shen, W. (2020). Shear velocity model of Alaska via joint inversion of Rayleigh wave ellipticity, phase velocities, and receiver functions across the Alaska transportable Array. *Journal of Geophysical Research: Solid Earth, 125*, e2019JB018582. https://doi.org/10.1029/2019JB018582

Boore, D. M., Gibbs, J. F., & Rodriguez, M. (2003). *A compendium of P-and S-wave velocities from surface-to-borehole logging: Summary and reanalysis of previously published data and analysis of unpublished data* (p. 13). US Department of the Interior, US Geological Survey. http://pubs.usgs.gov/of/2003/0191/.

Brocher, T. (2005). Empirical relations between elastic wavespeeds and density in the Earth's crust. *Bulletin of the Seismological Society of America, 95*(6), 2081–2092. https://doi.org/10.1785/0120050077

California Department of Water Resources (2017), SGMA Portal –GSA Formation Notification System, State of California Department of Water Resources. https://sgma.water.ca.gov/webgis/?appid=SGMADataViewer#gwlevels

Catchings, R. D., Rymer, M. J., Goldman, M. R., Sickler, R. R., & Criley, C. J. (2014). A method and example of seismically imaging near-surface fault zones in geologically complex areas using Vp, Vs, and their ratios. *Bulletin of the Seismological Society of America*, *104*(4), 1989-2006. https://doi.org/10.1785/0120130294

Catchings, R. D., Hernandez, J., Goldman, M. R., Chan, J. H., Sickler, R. R., Olson, B., & Criley, C. J. (2020). *2018 US Geological Survey–California Geological Survey Fault-Imaging Surveys Across the Hollywood and Santa Monica Faults, Los Angeles County, California* (No. 2020-1049). US Geological Survey. https://doi.org/10.3133/ofr20201049

Chen, P., Zhao, L., & Jordan, T. H. (2007). Full 3D tomography for the crustal structure of the Los Angeles region. *Bulletin of the Seismological Society of America*, *97*(4), 1094–1120. https://doi.org/10.1785/0120060222

Christensen, N. I. (1996). Poisson's ratio and crustal seismology. *Journal of Geophysical Research: Solid Earth*, *101*(B2), 3139-3156. https://doi.org/10.1029/95JB03446

Dreiling, J., Tilmann, F., Yuan, X., Haberland, C., & Seneviratne, S. W. M. (2020). Crustal structure of Sri Lanka derived from joint inversion of surface wave dispersion and receiver functions using a Bayesian approach. Journal of Geophysical Research: Solid Earth, 125, e2019JB018688. https://doi.org/10.1029/2019JB018688

Fang, H., Zhang, H., Yao, H., Allam, A., Zigone, D., Ben-Zion, Y., et al. (2016). A new algorithm for three-dimensional joint inversion of body wave and surface wave data and its application to the Southern California plate boundary region. *Journal of Geophysical Research: Solid Earth*, *121*, 3557–3569. https://doi.org/10.1002/2015JB012702

Fang, H., Yao, H., Zhang, H., Thurber, C., Ben-Zion, Y., & van der Hilst, R. D. (2019). Vp/Vs tomography in the southern California plate boundary region using body and surface wave traveltime data. *Geophysical Journal International, 216*(1), 609-620. https://doi.org/10.1093/gji/ggy458

Fletcher, J. B., & Erdem, J. (2017). Shear-wave velocity model from Rayleigh wave group velocities centered on the Sacramento/San Joaquin Delta. *Pure and Applied Geophysics*, *174*(10), 3825–3839. https://doi.org/10.1007/s00024-017-1587-x

Fliedner, M. M., Klemperer, S. L., & Christensen, N. I. (2000). Three-dimensional seismic model of the Sierra Nevada arc, California, and its implications for crustal and upper mantle composition. *Journal of Geophysical Research*, *105*(B5), 10,899–10,921. https://doi.org/10.1029/2000JB900029

Fuis, G. S., Ryberg, T., Godfrey, N. J., Okaya, D. A., & Murphy, J. M. (2001). Crustal structure and tectonics from the Los Angeles basin to the Mojave Desert, southern California. *Geology*, *29*(1), 15–18. https://doi.org/10.1130/0091-7613(2001)0292.0.CO;2

Fuis, G. S., Bauer, K., Goldman, M. R., Ryberg, T., Langenheim, V. E., Scheirer, D. S., et al. (2017). Subsurface geometry of the San Andreas Fault in Southern California: Results from the Salton Seismic Imaging Project (SSIP) and strong ground motion expectations. *Bulletin of the Seismological Society of America*, *107*(4), 1642–1662. https://doi.org/10.1785/0120160309

Gastil, R. G., Phillips, R. P., & Allison, E. C. (1975). *Reconnaissance geology of the state of Baja California* (Vol. 140). Geological Society of America.

Graves, R., Jordan, T. H., Callaghan, S., Deelman, E., Field, E., Juve, G., et al. (2011). CyberShake: A physics-based seismic hazard model for Southern California. *Pure and Applied Geophysics*, *168*(3–4), 367–381. https://doi.org/10.1007/s00024-010-0161-6

Han, L., Hole, J. A., Stock, J. M., Fuis, G. S., Kell, A., Driscoll, N. W., et al. (2016). Continental rupture and the creation of new crust in the Salton Trough rift, Southern California and northern Mexico: Results from the Salton Seismic Imaging Project. *Journal of Geophysical Research: Solid Earth*, 121, 7469–7489. https://doi.org/10.1002/2016JB013139

Hauksson, E. (2000). Crustal structure and seismicity distribution adjacent to the Pacific and North America plate boundary in southern California. *Journal of Geophysical Research: Solid Earth*, *105*(B6), 13875-13903. https://doi.org/10.1029/2000JB900016

Hauksson, E., & Haase, J. S. (1997). Three-dimensional VP and VP/VS velocity models of the Los Angeles basin and central Transverse Ranges, California. *Journal of Geophysical Research: Solid Earth*, *102*(B3), 5423-5453. https://doi.org/10.1029/96JB03219

Herrmann, R. B., & Ammon, C. J. (2004). Surface waves, receiver functions and crustal structure, in Computer Programs in Seismology, Version 3.30, Saint Louis University. Retrieved from http://www.eas.slu.edu/People/RBHerrmann/CPS330.html

Hildenbrand, T. G., Davidson, J. G., Ponti, D. J., & Langenheim, V. E. (2001). Implications for the formation of the Hollywood Basin from gravity interpretations of the northern Los Angeles Basin, California. *US Geological Survey, Open File Report*, *394*. https://pubs.usgs.gov/of/2001/0394/.

Irwin, W. (1990). Geologic and plate-tectonic development in the San Andreas fault system. *USGS Professional Paper 1515*, 61– 82. Retrieved from https://pubs.usgs.gov/pp/1990/1515/pp1515.pdf

Karato, S., & Jung, H. (1998). Water, partial melting and the origin of the seismic low velocity and high attenuation zone in the upper mantle. *Earth and Planetary Science Letters, 157*(3–4), 193–207. https://doi.org/10.1016/S0012-821X(98)00034-X

Kimbrough, D. L., Grove, M., & Morton, D. M. (2015). Timing and significance of gabbro emplacement within two distinct plutonic domains of the Peninsular Ranges batholith, southern and Baja California. *GSA Bulletin, 127*(1-2), 19-37. https://doi.org/10.1130/B30914.1

Langenheim, V. E., & Jachens, R. C. (2003). Crustal structure of the Peninsular Ranges batholith from magnetic data: Implications for Gulf of California rifting. *Geophysical Research Letters, 30*(11). https://doi.org/10.1029/2003GL017159

Langston, C. A. (1977). Corvallis, Oregon, crustal and upper mantle receiver structure from teleseismic P and S waves. *Bulletin of the Seismological Society of America, 67*(3), 713–724.

Langston, C. A. (1979). Structure under Mount Rainier, Washington, inferred from teleseismic body waves. *Journal of Geophysical Research, 84*(B9), 4749–4762. https://doi.org/10.1029/JB084iB09p04749

Lee, E. J., Chen, P., Jordan, T. H., Maechling, P. B., Denolle, M. A., & Beroza, G. C. (2014). Full-3-D tomography for crustal structure in southern California based on the scattering-integral and the adjoint-waveform methods. *Journal of Geophysical Research: Solid Earth, 119*, 6421–6451. https://doi.org/10.1002/2014JB011346

Li, G., Niu, F., Yang, Y., & Tao, K. (2019). Joint inversion of Rayleigh wave phase velocity, particle motion, and teleseismic body wave data for sedimentary structures. *Geophysical Research Letters, 46,* 6469–6478. https://doi.org/10.1029/2019GL082746

Ligorría, J. P., & Ammon, C. J. (1999). Iterative deconvolution and receiver-function estimation. *Bulletin of the Seismological Society of America, 89*(5), 1395–1400.

Lin, F.-C., Moschetti, M. P., & Ritzwoller, M. H. (2008). Surface wave tomography of the western United States from ambient seismic noise: Rayleigh and Love wave phase velocity maps. *Geophysical Journal International, 173*(1), 281–298. https://doi.org/10.1111/j.1365- 246X.2008.03720.x

Lin, F.-C., Tsai, V. C., & Schmandt, B. (2014). 3-D crustal structure of the western United States: Application of Rayleigh-wave ellipticity extracted from noise cross-correlations. *Geophysical Journal International, 198*(2), 656–670. https://doi.org/10.1093/gji/ggu160

Lin, G. (2020). Spatiotemporal variations of in situ Vp/Vs ratio within the Salton Sea Geothermal Field, southern California. *Geothermics*, *84*, 101740. https://doi.org/10.1016/j.geothermics.2019.101740

Lin, G., & Shearer, P. (2007). Estimating local Vp/Vs ratios within similar earthquake clusters. *Bulletin of the Seismological Society of America*, *97*(2), 379-388. https://doi.org/10.1785/0120060115

Lin, G., Shearer, P. M., Hauksson, E., & Thurber, C. H. (2007). A three-dimensional crustal seismic velocity model for southern California from a composite event method. *Journal of Geophysical Research: Solid Earth*, *112*(B11). https://doi.org/10.1029/2007JB004977

Lin, G., Thurber, C. H., Zhang, H., Hauksson, E., Shearer, P. M., Waldhauser, F., et al. (2010). A California statewide three-dimensional seismic velocity model from both absolute and differential times. *Bulletin of the Seismological Society of America, 100*(1), 225–240. https://doi.org/ 10.1785/0120090028

Livers, A. J., Han, L., Delph, J., White-Gaynor, A., Petit, R., Hole, J. A., et al. (2012). Tomographic characteristics of the northern geothermally active rift zone of the Imperial Valley and its rift margins: Salton seismic imaging project (SSIP). *AGU Fall Meet. Abstr.*

Lutter, W. J., Fuis, G. S., Ryberg, T., Okaya, D. A., Clayton, R. W., Davis, P. M., et al. (2004). Upper crustal structure from the Santa Monica Mountains to the Sierra Nevada, Southern California: Tomographic results from the Los Angeles Regional Seismic Experiment, Phase II (LARSE II). *Bulletin of the Seismological Society of America, 94*(2), 619–632. https://doi.org/10.1785/0120030058

Ma, Y., & Clayton, R. W. (2016). Structure of the Los Angeles Basin from ambient noise and receiver functions. *Geophysical Journal International*, *206*(3), 1645–1651. https://doi.org/10.1093/gji/ggw236

Magistrale, H., McLaughlin, K., & Day, S. (1996). A geology-based 3D velocity model of the Los Angeles basin sediments. *Bulletin of the Seismological Society of America, 86*(4), 1161–1166.

McCaffree Pellerin, C. L., and N.I. Christensen, Interpretation of crustal seismic velocities in the San Gabriel-Mojave region, southern California. *Tectonophysics, 286*, 253-271, 1998

Mitchell, T. M., & Faulkner, D. R. (2009). The nature and origin of off-fault damage surrounding strike-slip fault zones with a wide range of displacements: A field study from the Atacama fault system, northern Chile. *Journal of Structural Geology*, *31*(8), 802-816. https://doi.org/10.1016/j.jsg.2009.05.002

Morton, D. M., & Kennedy, M. P. (2005). Preliminary Geologic Map of the Sage 7.50 Quadrangle, Riverside County, California, (Map No. 2005– 1285). United States Geological Survey. Retrieved from http://pubs.usgs.gov/of/2005/1285/

Murphy, J. M., Fuis, G. S., Ryberg, T., Lutter, W. J., Catchings, R. D., & Goldman, M. R. (2010). Detailed P-and S-Wave Velocity Models along the LARSE II Transect, Southern California. *Bulletin of the Seismological Society of America, 100*(6), 3194-3212. https://doi.org/10.1785/0120090004

Ojo, A. O., Ni, S., Xie, J., & Zhao, L. (2019). Further constraints on the shear wave velocity structure of Cameroon from joint inversion of receiver function, Rayleigh wave dispersion and ellipticity measurements. *Geophysical Journal International*, *217*(1), 589-619. https://doi.org/10.1093/gji/ggz008

Park, J., & Levin, V. (2016). Anisotropic shear zones revealed by backazimuthal harmonics of teleseismic receiver functions. *Geophysical supplements to the monthly notices of the Royal Astronomical Society, 207*(2), 1216–1243. https://doi.org/10.1093/gji/ggw323

Plesch, A., Shaw, J. H., Benson, C., Bryant, W. A., Carena, S., Cooke, M., et al. (2007). Community fault model (CFM) for southern California. *Bulletin of the Seismological Society of America, 97*(6), 1793–1802. https://doi.org/10.1785/0120050211

Qiu, H., Lin, F. C., & Ben-Zion, Y. (2019). Eikonal tomography of the Southern California plate boundary region. *Journal of Geophysical Research: Solid Earth*, *124*(9), 9755-9779. https://doi.org/ 10.1029/2019JB017806

Roy, C., & Romanowicz, B. A. (2017). On the implications of a priori constraints in transdimensional Bayesian inversion for continental lithospheric layering. *Journal of Geophysical Research: Solid Earth*, *122*, 10,118–10,131. https://doi.org/10.1002/2017JB014968

Sauber, J., Thatcher, W., & Solomon, S. C. (1986). Geodetic measurement of deformation in the central Mojave Desert, California. *Journal of Geophysical Research: Solid Earth*, *91*(B12), 12683-12693. https://doi.org/10.1029/JB091iB12p12683

Schmandt, B., & Humphreys, E. (2010). Seismic heterogeneity and small-scale convection in the southern California upper mantle. *Geochemistry, Geophysics, Geosystems, 11,* Q05004. https://doi.org/10.1029/2010GC003042

Schulte-Pelkum, V., & Mahan, K. H. (2014a). A method for mapping crustal deformation and anisotropy with receiver functions and first results from USArray. *Earth and Planetary Science Letters, 402*, 221–233.

Schulte-Pelkum, V., & Mahan, K. H. (2014b). Imaging faults and shear zones using receiver functions. *Pure and Applied Geophysics, 171*(11), 2967–2991. https://doi.org/10.1007/s00024-014-0853-4

Schulte-Pelkum, V., Mahan, K. H., Shen, W., & Stachnik, J. C. (2017). The distribution and composition of high-velocity lower crust across the continental US: Comparison of seismic and xenolith data and implications for lithospheric dynamics and history. *Tectonics, 36*, 1455–1496. https://doi.org/10.1002/2017TC004480

Shaw, J. H., Plesch, A., Tape, C., Suess, M. P., Jordan, T. H., Ely, G., ... & Olsen, K. (2015). Unified structural representation of the southern California crust and upper mantle. *Earth and Planetary Science Letters, 415*, 1-15. https://doi.org/10.1016/j.epsl.2015.01.016

Shearer, P. M. (1988). Cracked media, Poisson's ratio and the structure of the upper oceanic crust. *Geophysical Journal International*, *92*(2), 357-362. https://doi.org/10.1111/j.1365-246X.1988.tb01149.x

Shen, W., & Ritzwoller, M. H. (2016). Crustal and uppermost mantle structure beneath the United States. *Journal of Geophysical Research: Solid Earth, 121*, 4306–4342. https://doi.org/10.1002/2016JB012887

Shen, W., Ritzwoller, M. H., Schulte-Pelkum, V., & Lin, F. C. (2012). Joint inversion of surface wave dispersion and receiver functions: A Bayesian Monte-Carlo approach. *Geophysical Journal International, 192*(2), 807–836. https://doi.org/10.1093/gji/ggs050

Süss, M. P., & Shaw, J. H. (2003). P wave seismic velocity structure derived from sonic logs and industry reflection data in the Los Angeles basin, California. *Journal of Geophysical Research: Solid Earth*, *108*(B3). https://doi.org/10.1029/2001JB001628

Taborda, R., Azizzadeh-Roodpish, S., Khoshnevis, N., & Cheng, K. (2016). Evaluation of the southern California seismic velocity models through simulation of recorded events. *Geophysical Journal International, 205*(3), 1342–1364. https://doi.org/10.1093/gji/ggw085

Tanimoto, T., & Prindle Sheldrake, K. (2002). Three-dimensional S-wave velocity structure in southern California. *Geophysical Research Letters*, *29*(8), 1223. https://doi.org/10.1029/2001GL013486

Tape, C., Liu, Q., Maggi, A., & Tromp, J. (2010). Seismic tomography of the southern California crust based on spectral-element and adjoint methods. *Geophysical Journal International, 180*(1), 433–462. https://doi.org/10.1111/j.1365-246X.2009.04429.x

Vidale, J. E., & Helmberger, D. V. (1988). Elastic finite-difference modeling of the 1971 San Fernando, California earthquake. *Bulletin of the Seismological Society of America, 78*(1), 122–141.

Vinnik, L. P. (1977). Detection of waves converted from P to SV in the mantle. *Physics of the Earth and Planetary Interiors, 15*(1), 39–45. https://doi.org/10.1016/0031-9201(77)90008-5

Water Replenishment District of Southern California (2017), Regional Groundwater Monitoring Report Central Basin and West Coast Basin Los Angeles County, California https://www.wrd.org/sites/pr/files/2015-16%20RGWMR%20Final.pdf

Ward, K. M., & Lin, F. C. (2018). Lithospheric structure across the Alaskan cordillera from the joint inversion of surface waves and receiver functions. *Journal of Geophysical Research: Solid Earth, 123*(10), 8780–8797. https://doi.org/10.1029/2018JB015967

Wetmore, P. H., Herzig, C., Alsleben, H., Sutherland, M., Schmidt, K. L., Schultz, P. W., ... & Kimbrough, D. L. (2003). Mesozoic tectonic evolution of the Peninsular Ranges of southern and Baja California. *SPECIAL PAPERS-GEOLOGICAL SOCIETY OF AMERICA*, *374*, 93-116.

Wills, C. J., & Clahan, K. B. (2006). Developing a map of geologically defined site-condition categories for California. *Bulletin of the Seismological Society of America, 96*(4A), 1483-1501. https://doi.org/10.1785/0120050179

Yang, J., & Sato, T. (2000). Interpretation of seismic vertical amplification observed at an array site. *Bulletin of the Seismological Society of America*, *90*(2), 275-285. https://doi.org/10.1785/0119990068

Yeck, W. L., Sheehan, A. F., & Schulte-Pelkum, V. (2013). Sequential H-κ stacking to obtain accurate crustal thicknesses beneath sedimentary basins. *Bulletin of the Seismological Society of America, 103*(3), 2142–2150. https://doi.org/10.1785/0120120290

Zaitsev, V. Y., Radostin, A. V., Pasternak, E., & Dyskin, A. (2017). Extracting real-crack properties from non-linear elastic behaviour of rocks: abundance of cracks with dominating normal compliance and rocks with negative Poisson ratios. *Nonlinear Processes in Geophysics*, *24*(3), 543. https://doi.org/10.5194/npg-24-543-2017

Zhang, Q., & Lin, G. (2014). Three-dimensional Vp and Vp/Vs models in the Coso geothermal area, California: Seismic characterization of the magmatic system. *Journal of Geophysical Research: Solid Earth*, *119*(6), 4907-4922. https://doi.org/10.1002/2014JB010992

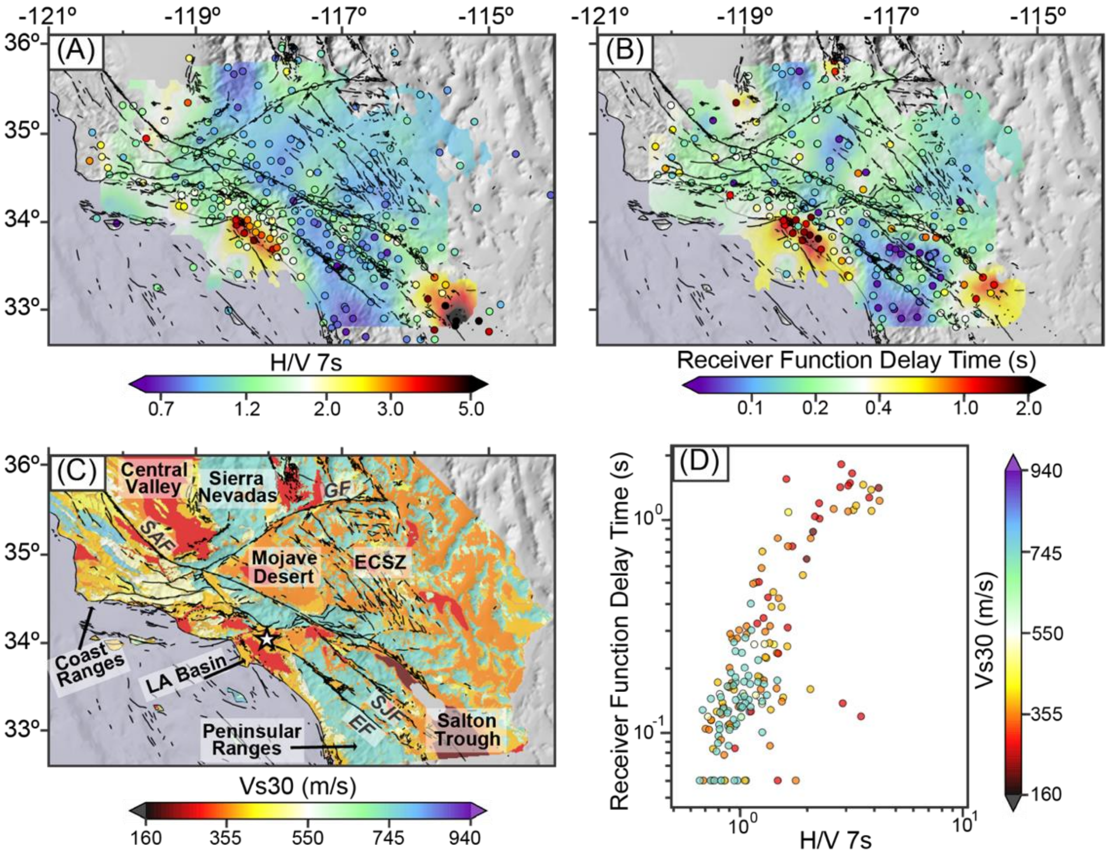

Figure 1. Maps showing data at each station (circle) and Gaussian-smoothed, with ¾ width corresponding to the distance to the nearest three stations, onto the underlying map for **(a)** H/V at 7 s period and **(b)** receiver function initial pulse delay time. **(c)** Vs30 map (Wills & Clahan, 2006) with station RUS marked as a star and main geological features and major faults labeled, including the San Andreas (SAF), Garlock (GF), San Jacinto (SJF), and Elsinore (EF) faults. **(d)** Scatter plot of each station's H/V at 7 s period and receiver function delay time (s) from (a) and (b), colored according to the Vs30 (m/s) nearest to that station.

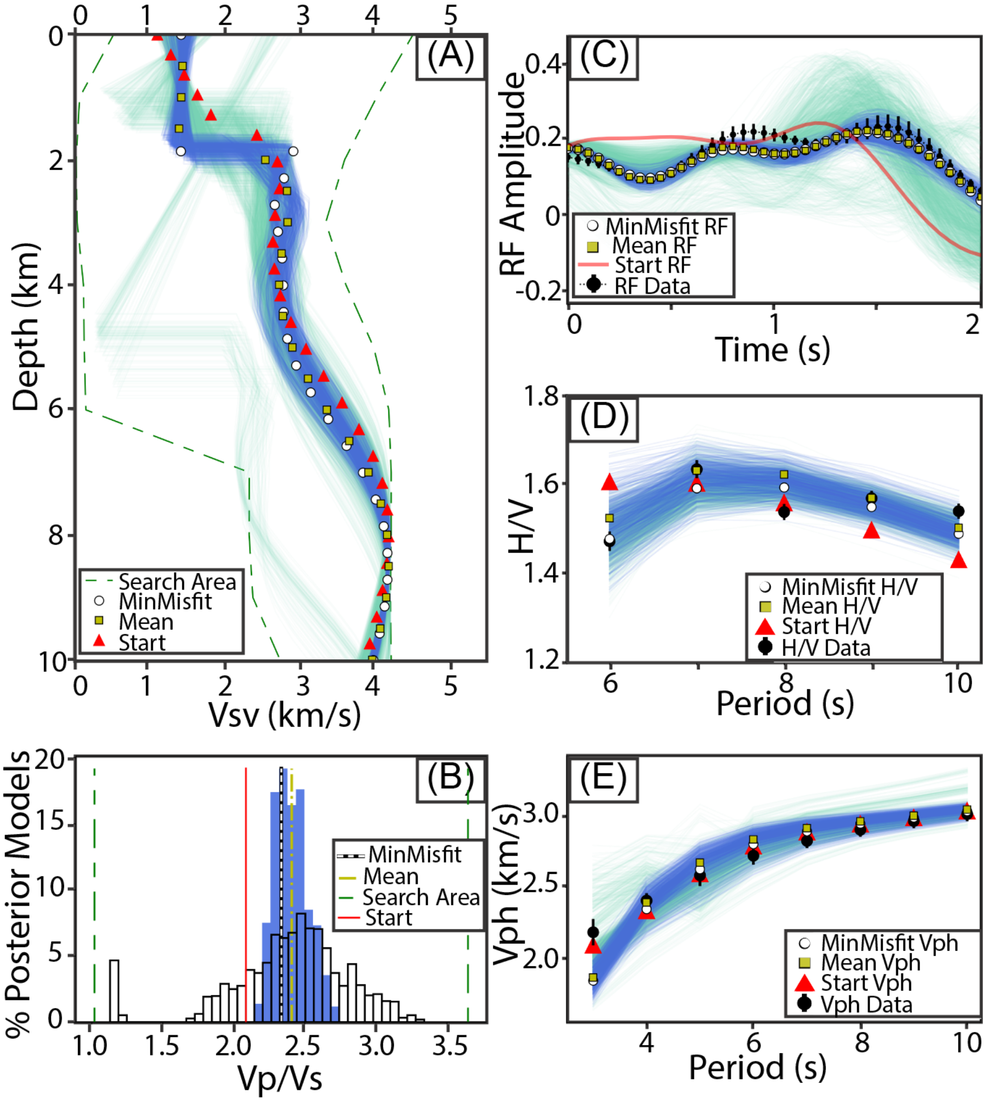

Figure 2. MCMC joint inversion results for station RUS (white star, Figure 1c) including **(a, b)** search area (green dashed lines), posterior results when incorporating Rayleigh-wave phase velocity and H/V data only ((a) light green or (b) transparent) and all datasets (blue), as well as the starting model (red), minimum misfit model from the posterior (white), and mean model from the posterior (yellow) for both (a) shear velocity (Vs) results of the top 10km and (b) Vp/Vs results of the top linear layer. Data (black) and forward model results for the posterior sets, starting, mean, and minimum misfit models for **(c)** receiver functions, **(d)** H/V, and **(e)** phase velocities.

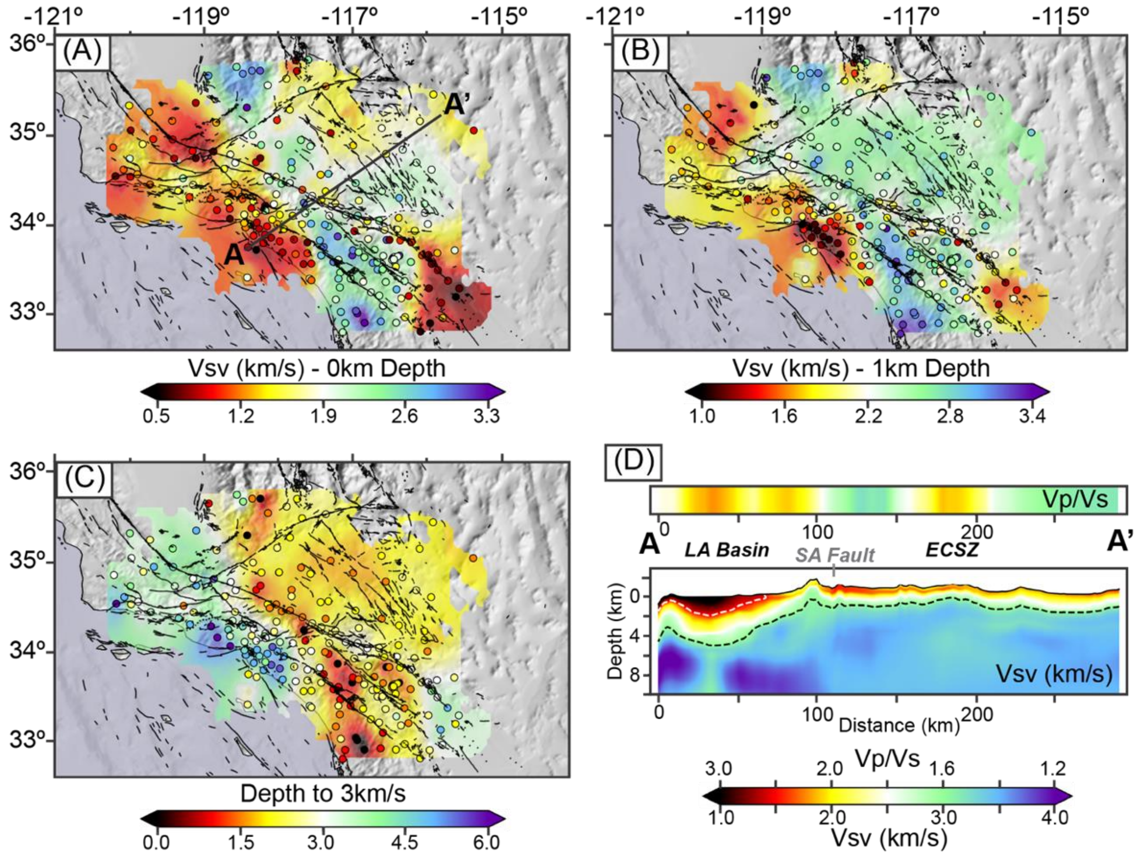

Figure 3. Vs results at each station, with Gaussian-smoothed (see Figure 1 description) underlying map, at **(a)** the surface and **(b)** 1 km depths, and **(c)** depth to 3 km/s. **(d)** Cross-section A-A’ for Vp/Vs ratio in the top linear layer (top) and Vs to 10 km depth (bottom), including white dashed line at 1.5 km/s and black dashed line at 3 km/s.

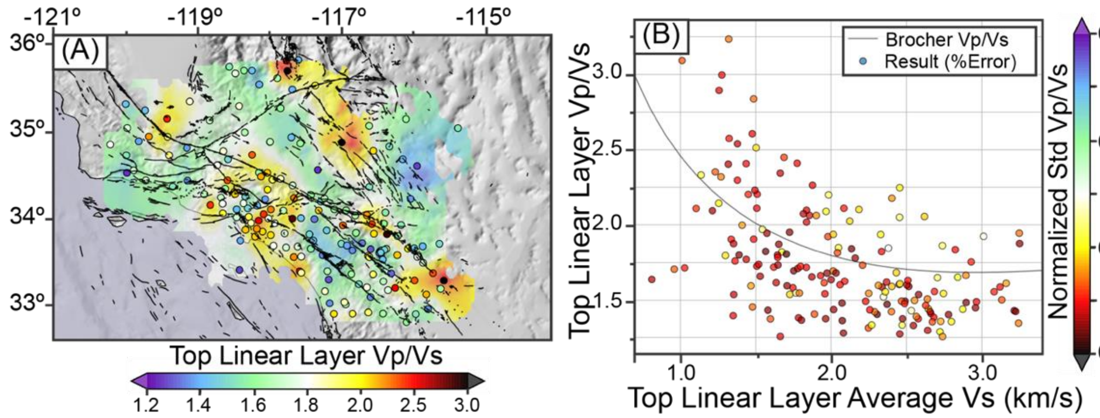

Figure 4. Vp/Vs results from the top linear layer as a **(a)** map at each station, with Gaussian-smoothed (see Figure 1 description) underlying map, and **(b)** scatter plot from each station of average Vs in the top linear layer versus Vp/Vs of the top linear layer.

Figure1.

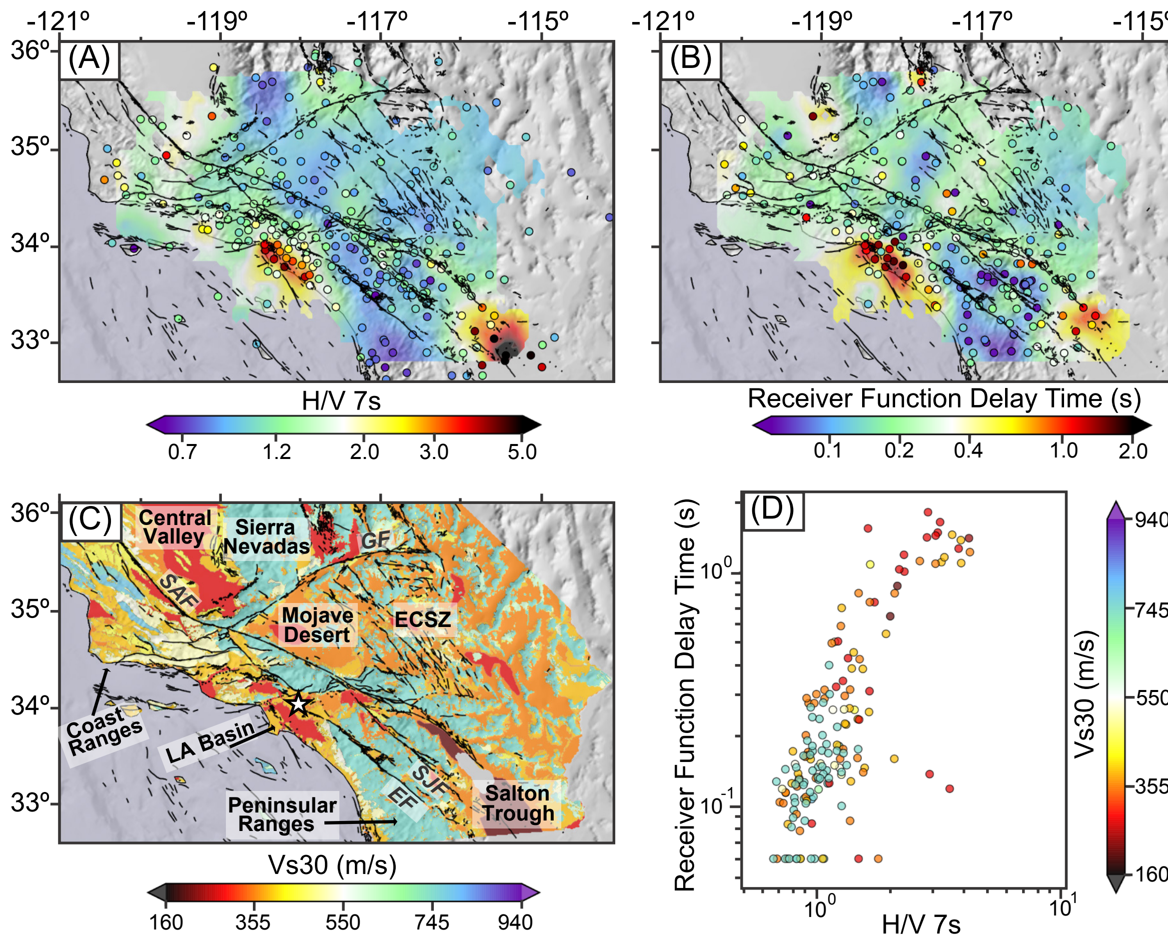

(A)
H/V 7s
0.7
1.2
2.0
3.0
5.0
(B)
Receiver Function Delay Time (s)
0.1
0.2
0.4
1.0
2.0
-121º
-119º
-117º
-115º
36º
35º
34º
33º
(C)
Central Valley
Sierra Nevadas
GF
SAF
Mojave Desert
ECSZ
Coast Ranges
LA Basin
SJF
EF
Peninsular Ranges
Salton Trough
Vs30 (m/s)
160
355
550
745
940
(D)
Receiver Function Delay Time (s)
H/V 7s
Vs30 (m/s)

Figure2.

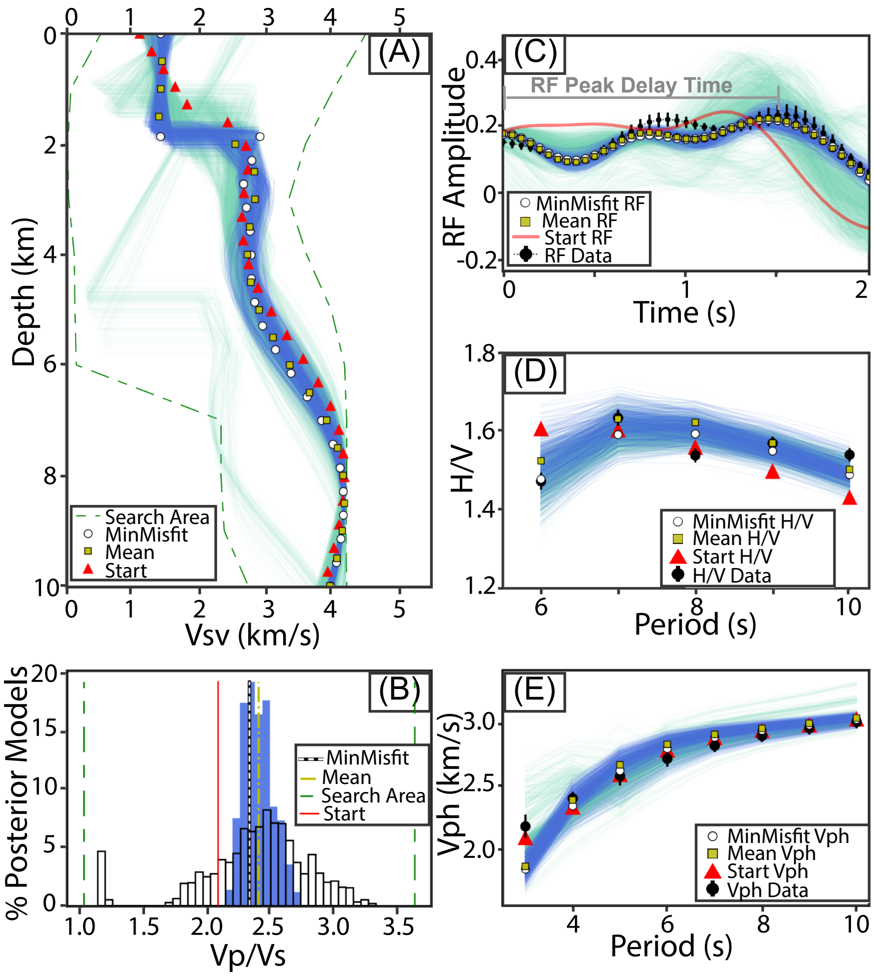

(A)
Depth (km)
Vsv (km/s)
Search Area
MinMisfit
Mean
Start
(B)
% Posterior Models
Vp/Vs
MinMisfit
Mean
Search Area
Start
(C)
RF Peak Delay Time
RF Amplitude
Time (s)
MinMisfit RF
Mean RF
Start RF
RF Data
(D)
H/V
Period (s)
MinMisfit H/V
Mean H/V
Start H/V
H/V Data
(E)
Vph (km/s)
Period (s)
MinMisfit Vph
Mean Vph
Start Vph
Vph Data

Figure3.

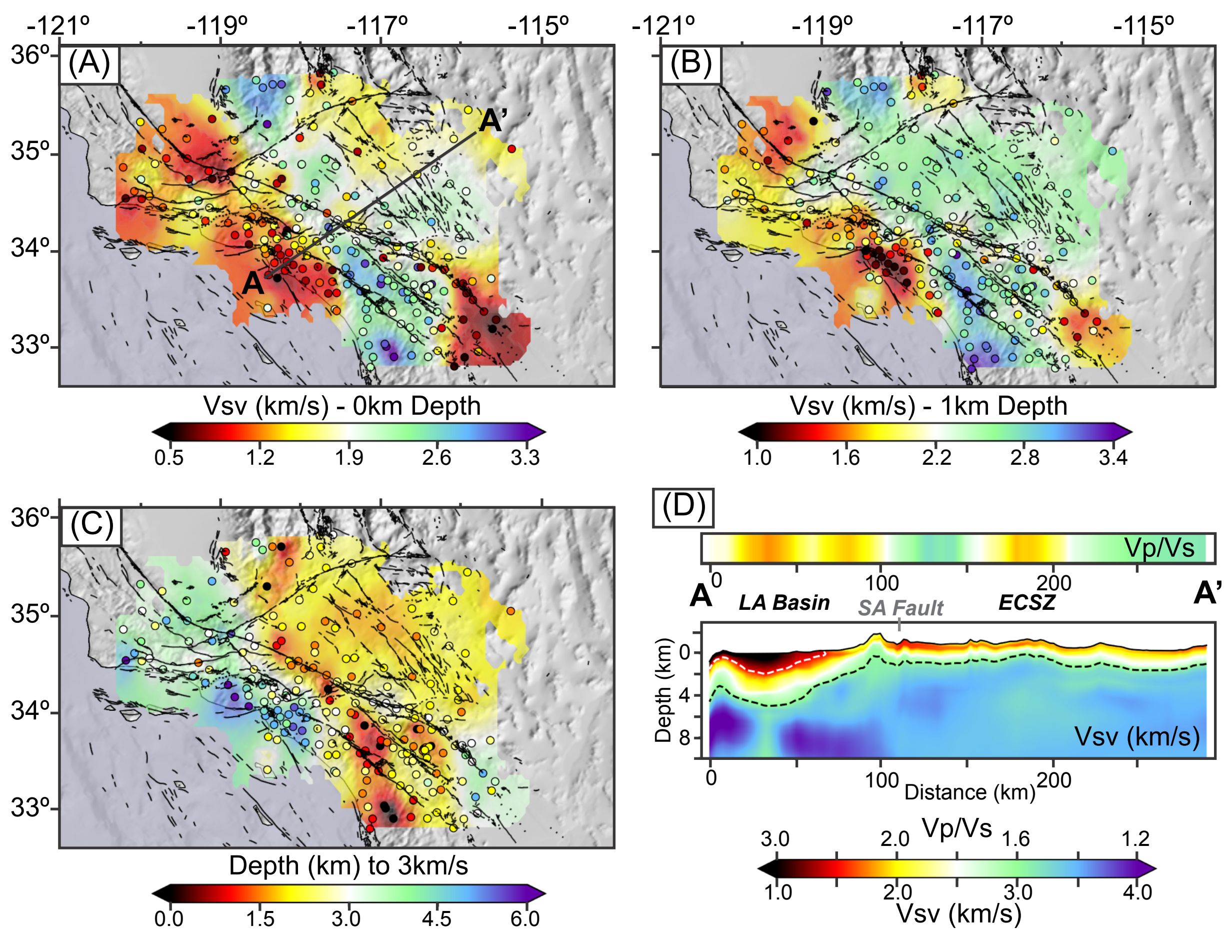

(A)
(B)
(C)
(D)
-121º
-119º
-117º
-115º
36º
35º
34º
33º
A
A'
Vsv (km/s) - 0km Depth
0.5
1.2
1.9
2.6
3.3
Vsv (km/s) - 1km Depth
1.0
1.6
2.2
2.8
3.4
Depth (km) to 3km/s
0.0
1.5
3.0
4.5
6.0
Vp/Vs
0
100
200
LA Basin
SA Fault
ECSZ
Depth (km)
Vsv (km/s)
Distance (km)
Vp/Vs
3.0
2.0
1.6
1.2
1.0
2.0
3.0
4.0
Vsv (km/s)

Figure4.

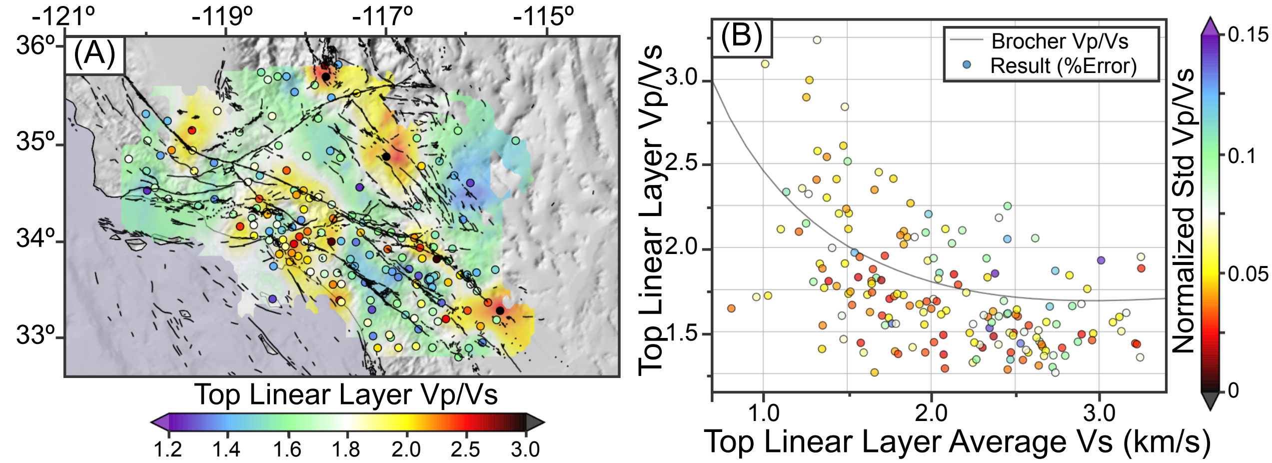

(A)
-121º
-119º
-117º
-115º
36º
35º
34º
33º
Top Linear Layer Vp/Vs
1.2
1.4
1.6
1.8
2.0
2.5
3.0
(B)
Brocher Vp/Vs
Result (%Error)
Top Linear Layer Vp/Vs
3.0
2.5
2.0
1.5
1.0
2.0
3.0
Top Linear Layer Average Vs (km/s)
Normalized Std Vp/Vs
0.15
0.1
0.05
0